Research Square

Preprints are preliminary reports that have not undergone peer review.
They should not be considered conclusive, used to inform clinical practice,
or referenced by the media as validated information.

Mechanical Design Guidelines for Perforated 3D Porous Metallic Bone Implants: Resolving the Stress-Shielding, Fatigue, and Permeability Trade-Off Around Fixation Tunnels

Guangtao Wei

guangtao19872206@163.com

Fujian Agriculture and Forestry University https://orcid.org/0000-0001-8266-9776

Miao Yu

Fujian Agriculture and Forestry University

Jun Liu

Fujian Provincial Cancer Hospital

Research Article

Keywords:

Posted Date: November 25th, 2026

DOI: https://doi.org/10.21203/rs.3.rs-11872441/v1

License: This work is licensed under a Creative Commons Attribution 4.0 International License.
Read Full License

Additional Declarations: The authors declare no competing interests.

Mechanical Design Guidelines for Perforated 3D Porous Metallic Bone Implants: Resolving the Stress-Shielding, Fatigue, and Permeability Trade-Off Around Fixation Tunnels

Guangtao Wei[1,*], **Miao Yu**[1], **Jun Liu**[2,*]

[1] College of Mechanical and Electrical Engineering, Fujian Agriculture and Forestry University, Fuzhou 350002, China

[2] Department of Medical Oncology, Clinical Oncology School of Fujian Medical University, Fujian Cancer Hospital, Fuzhou 350014, China

[*] Corresponding authors: Guangtao Wei (wgt@hrbeu.edu.cn); Jun Liu (liujun@fjzlhospital.cn)

Abstract

Three-dimensional (3D) additively manufactured porous metallic bone implants—such as patient-specific pelvic, acetabular, and metaphyseal prostheses—are rarely unperforated periodic lattices in clinical service. Instead, they must accommodate $\text{Ø}3.5-6.5$ mm locking screw tunnels, K-wire trajectories, and bone-graft fenestrations that sever load-bearing trabecular struts and distort physiological strain transfer to host bone. Current clinical practice relies on dense metallic fixation wings or surrounds each fixation hole in a porous wing with a $1.0-2.0$ mm solid titanium boss; however, quantitative multi-physics benchmarks remain lacking. Here we demonstrate via 310,698-DOF 3D continuum elasticity, Crossland multi-axial high-cycle fatigue analysis, and 3D pore-scale Darcy seepage simulations that conventional solid screw bosses create a counterproductive **mechanical–biological paradox**: they worsen far-field 3D strain distortion beyond even an unreinforced hole ($J_{3D} = 1.073$ vs. 1.000), add $+10.7\%-19.4\%$ titanium mass that aggravates postoperative imaging artifacts, and completely occlude radial peri-screw vascular permeability ($k_r = 0$). To replace empirical solid sleeves without requiring patient-by-patient 3D topology optimization, we establish **four closed-form engineering design guidelines** grounded in a 20-architecture 3D perforation scaling law ($r^2 = 0.989$ continuum–lattice parity) and 3D vector spherical harmonic interface mechanics. Across columnar buttress lattices and clinical orthopedic Diamond ($Z = 4$) tetrahedral scaffolds, open-pore node-flared bypass cloaks cut 3D field distortion by $28.5\%-53.0\%$, lower peak Crossland fatigue stress by $8.1\%-14.1\%$ below bare holes with zero added mass, and preserve native-bone-level radial permeability (3.95×10^{-8} m^2). Monte Carlo laser powder bed fusion (LPBF) tolerance audits ($\sigma_d = 38\ \mu$m, $\pm 80\ \mu$m etching, 0.4 mm drill eccentricity) confirm a 100% $(80/80)$ win-win pass rate, while multi-activity gait sweeps ($0^\circ-90^\circ$) demonstrate omnidirectional stability ($J_{3D} \leq 0.50$) where single-load optimization fails ($J_{3D} \to 1.61$). In a 3D anatomical human right hemipelvis reconstruction (Enneking Type II resection, 2,380 N Bergmann load) coupled to a 5,213-strut explicit Diamond iliac wing sub-model, our zero-optimization design outperforms all three representative traditional clinical practices—slashing periprosthetic stress shielding from 69.8% (solid Ti plate) and 64.0% (solid-boss wing) to 4.0%, elevating Frost homeostasis from $25.6\%-31.5\%$ to 86.8%, cutting explicit trabecular Crossland fatigue stress by -40.6% below solid-boss weld roots ($170.0 \to 101.0$ MPa) and -18.2% below bare holes ($123.5 \to 101.0$ MPa), and holding osteotomy micromotion to $6.0\ \mu$m.

Finally, cross-regime validation on a **Regime II** orthotropic lumbar vertebral corpectomy endoprosthesis (ORTHO_TRAB_A, $\lambda_3 = 8.68$) confirms identical zero-optimization performance (96.6% vertebral homeostasis, 2.5% endplate overload, -34.3% fatigue stress vs. solid bosses).

Keywords: 3D-printed porous titanium implants; Pelvic tumor endoprosthesis; Fixation screw tunnels; Stress shielding; Multi-axial fatigue; Osteogenic permeability; Elastic cloaking

Statement of Significance

Additively manufactured 3D porous metallic bone prostheses are routinely pierced by locking screw tunnels and graft windows, yet current clinical designs rely on empirical 1–2 mm solid titanium screw bosses that inadvertently worsen 3D strain distortion, induce 64%–70% periprosthetic bone stress shielding, concentrate weld-root fatigue stress, and completely seal peri-screw nutrient transport. Conversely, patient-specific 3D topology optimization around every oblique screw channel is computationally prohibitive and fails when daily gait activities rotate joint loads. This work establishes four closed-form, zero-optimization CAD guidelines—combining equal-mass open-pore corridors, node-flared tetrahedral Diamond bypass struts, inter-screw spacing bounds, and supra-osteotomy buffers—that restore 87% physiological bone homeostasis, cut trabecular fatigue stress by 41% vs. solid bosses, and preserve native radial permeability across 100% of LPBF manufacturing tolerance audits.

1. Introduction

Laser powder bed fusion (LPBF) and electron beam melting (EBM) of Ti-6Al-4V and tantalum alloys have transformed the reconstruction of large segmental and cavitary bone defects following pelvic tumor resection, revision arthroplasty, and complex trauma [1–4]. By tailoring relative density $\bar{\rho} \equiv \rho_0 \in [0.15, 0.35]$ and unit-cell architecture—most notably bending-dominated tetrahedral Diamond ($Z = 4$), triply periodic minimal surface (TPMS) Gyroid, stochastic Voronoi trabecular networks, and orthotropic buttress columns—engineers match the apparent modulus of an *intact* porous scaffold ($1.5–15$ GPa) to regional host bone [5–8].

In clinical service, however, load-bearing prostheses are never unperforated periodic blocks: they must be pierced by $Ø3.5–6.5$ mm locking screw tunnels, K-wire guides, and $Ø6–10$ mm autograft fenestrations [9,10]. Introducing these millimeter-scale perforations exposes pervasive **clinical design blind spots** (**Fig. 1**):

1. **Blind Spot 1 — Unreinforced ("Bare") Screw Holes (Trad-3, Fig. 1a):** Cutting directly through a porous lattice severs primary load-bearing struts, triggering $+26.5\%$ local multi-axial fatigue hotspots at cut strut roots while distorting macroscopic strain transfer across adjacent osteotomies ($J_{3D} = 1.000$).

2. **Blind Spot 2 — Dense Plates (Trad-1) and Solid Titanium Screw Bosses (Trad-2, Fig. 1b,d):** Retaining a dense wrought/SLM Ti-6Al-4V fixation plate ($E_s \approx 110$ GPa) or fusing a $1.0–2.2$ mm solid metallic sleeve around every screw bore in a porous wing implants rigid inclusions ($20\times–60\times$ stiffer than surrounding trabeculae) that trigger severe periprosthetic stress shielding, worsen 3D far-field strain distortion beyond even a bare hole ($J_{3D} = 1.073$), add $+10.7\%–308\%$ dead metallic mass that intensifies postoperative CT/MRI bloom artifacts critical to oncological surveillance, concentrate weld-root notch stress where slender struts meet rigid sleeves, and seal 100% of radial peri-screw nutrient transport ($k_r = 0$).

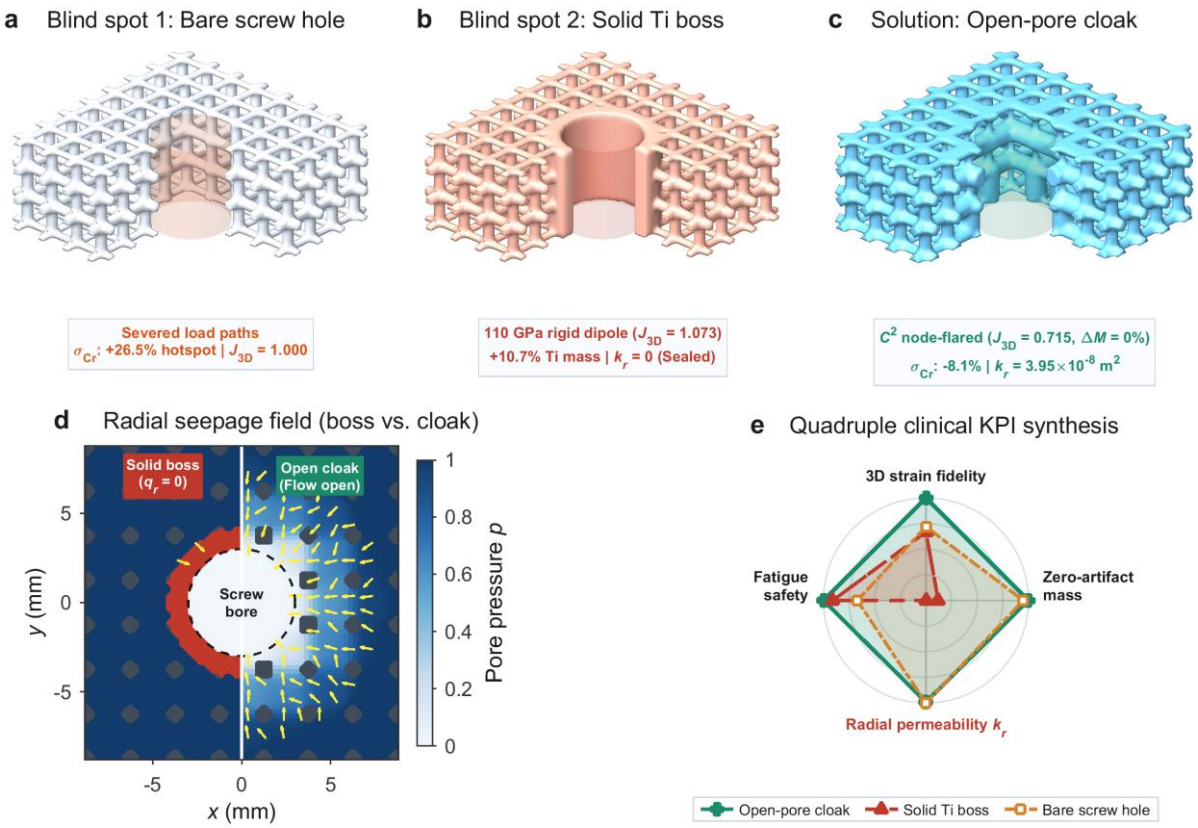


Figure 1. Industry blind spots in perforated 3D bone implants versus the proposed open-pore cloaking solution. (a–c) Three-quarter cutaway 3D implicit-SDF metallic renderings of (a) an unreinforced bare screw hole (G2), (b) a commercial solid titanium screw boss (G0, 1.05 mm dense wall), and (c) the proposed C^2 node-flared open-pore cloak (G3). (d) Split-screen mid-plane 3D Darcy pore-pressure p and radial velocity vectors: the solid boss blocks inward nutrient flux ($q_r = 0$, left), whereas the open-pore cloak maintains continuous radial seepage into the screw–bone interface (right). (e) Quadruple clinical KPI synthesis.

Meanwhile, bespoke 3D continuum topology optimization (10^5–10^7 DOFs) around every inclined screw hole in patient-specific CAD is computationally prohibitive, pinches bypass joint necks ($d_e < d_m$, **Supplementary Note S3** and **Fig. S3**), and over-fits a single nominal load vector—degrading sharply when daily gait activities rotate hip contact forces across walking, stair climbing, and chair rising. While 2D mechanical cloaking has restored planar compliance around plate cutouts [11–15]—including recent analytical outer-edge impedance matching and mass-neutral planar lattice width-grading principles [16,17]—3D bone implants introduce distinct volumetric corridor bounds, out-of-plane screw-tightening torsional interface floors (**Supplementary Note S1** and **Fig. S1**), tetrahedral joint-bending fatigue, LPBF geometric tolerances, and osteogenic permeability constraints [18–21]. Here we establish **four closed-form, zero-optimization CAD guidelines** (**Fig. 1c–e**) verified from 20-topology homogenization, 310k-DOF Hex8 elasticity, LPBF Monte Carlo tolerance audits, and multi-activity gait envelopes up to coupled 3D right-hemipelvis FEA and 5,213-strut explicit Diamond sub-modeling against all three traditional clinical practices.

2. Design Principles and Multi-Physics Evaluation Framework

Redistributing the solid volume excavated from a cylindrical screw tunnel or 3D spherical/ovoid graft cavity of radius $r_v = D_{\text{hole}}/2$ into a coaxial/concentric cloak corridor $r \in [r_v, r_c]$ at exact mass neutrality ($\Delta M = 0$) under an osteogenic upper relative-density ceiling $\rho(\mathbf{x}) \leq \rho_{\max}$ (enforcing minimum clear pore

throat $w_{\mathrm{pore}} \geq 600\,\mu$m [19]) from baseline relative density $\bar{\rho} \equiv \rho_0$ yields exact geometric feasibility bounds (**Rule 1**):

$$\begin{aligned} \frac{r_c}{r_v} &\geq \left(1 - \frac{\bar{\rho}}{\rho_{\max}}\right)^{-1/2} \quad \text{(3D cylindrical screw tunnel)}, \quad \frac{r_c}{r_v} \\ &\geq \left(1 - \frac{\bar{\rho}}{\rho_{\max}}\right)^{-1/3} \quad \text{(3D spherical graft cavity)}. \end{aligned} \tag{1}$$

In tetrahedral Diamond ($Z = 4$), bending moments peak at nodal joints ($s = 0, L$) and vanish at mid-span ($s = L/2$); introducing a **node-flared (dog-bone) profile** $d_e = \eta_{\mathrm{flare}}\, d_m$ ($\eta_{\mathrm{flare}} \in [1.18, 1.32]$) expands joint section modulus as η_{flare}^3, simultaneously restoring far-field compliance and reducing peak strut Crossland multi-axial high-cycle fatigue equivalent stress [22]:

$$\sigma_{\mathrm{Cr},i} = \sqrt{J_{2,a,i}} + \alpha_{\mathrm{Cr}}\, p_{\max,i} \leq \sigma_{\mathrm{Cr,lim}}, \quad \sqrt{J_{2,a,i}} = \frac{1-R}{2}\sqrt{\frac{\sigma_{\mathrm{tot},i}^2}{3} + \tau_{t,i}^2}, \quad p_{\max,i} = \frac{\sigma_{\mathrm{tot},i}}{3}, \tag{2}$$

where $R = 0.1$ is the physiological gait load ratio, $\alpha_{\mathrm{Cr}} = 0.32$ is the Ti-6Al-4V hydrostatic pressure sensitivity, $\sigma_{\mathrm{tot},i}$ is the total axial-plus-bending normal stress (scaled by notch factor K_f), $\tau_{t,i}$ is the torsional shear stress, and $\sigma_{\mathrm{Cr,lim}} = 175$ MPa is the 10^7-cycle as-printed LPBF Ti-6Al-4V ELI trabecular endurance limit. Near host osteotomies, positive Gaussian curvature ($K_G = 1/r^2 > 0$) excites spheroidal and purely 3D toroidal screw-twist interface floors (**Supplementary Note S1** and **Fig. S1**), suppressed exponentially via an unperforated, host-matched porous transition buffer of thickness $t_{\mathrm{buf}} \geq 1.5\,a$ (typically $1.5\text{–}2.0\,a$, where a is the unit-cell pitch; **Rule 4**). Full numerical protocols are provided in **Supplementary Notes S2–S6**.

3. Results and Quantitative Engineering Guidelines

3.1 Universal 3D Perforation Selection Map Across 20 Porous Architectures

Evaluating 20 periodic cubic, polyhedral foam, skeletal TPMS (Gyroid $I4_132$), clinical tetrahedral (Diamond $Z = 4$), orthotropic buttress, and stochastic 3D Laguerre–Voronoi supercells (**Fig. S2** and **Table S1**) reveals that macroscopic shear-to-axial perforation sensitivity $\Delta_\gamma/\Delta_\varepsilon$ (the ratio of apparent shear stiffness loss Δ_γ to uniaxial compressive stiffness loss Δ_ε caused by an unreinforced cavity) collapses onto (**Fig. 2a**):

$$\frac{\Delta_\gamma}{\Delta_\varepsilon} \approx \frac{2.46}{\lambda_3}, \quad \lambda_3 = \frac{\sqrt{C_{11}C_{22}}}{C_{66}} \quad (r^2 = 0.911 \text{ across all 20 3D networks}), \tag{3}$$

where $C_{11}, C_{22}, C_{12}, C_{66}$ are the homogenized 3D orthotropic/cubic stiffness components and $A_Z = 2C_{66}/(C_{11} - C_{12})$ is the Zener anisotropy ratio, with **discrete-to-continuum parity** $r^2 = 0.989$ (**Fig. 2b**). This scaling cleanly separates **Regime I** ($\lambda_3 \leq 4.5$, bending-dominated and TPMS scaffolds requiring node-flared cloaks) from **Regime II** ($\lambda_3 > 4.5$, columnar buttresses requiring tangential bypass with neck protection).

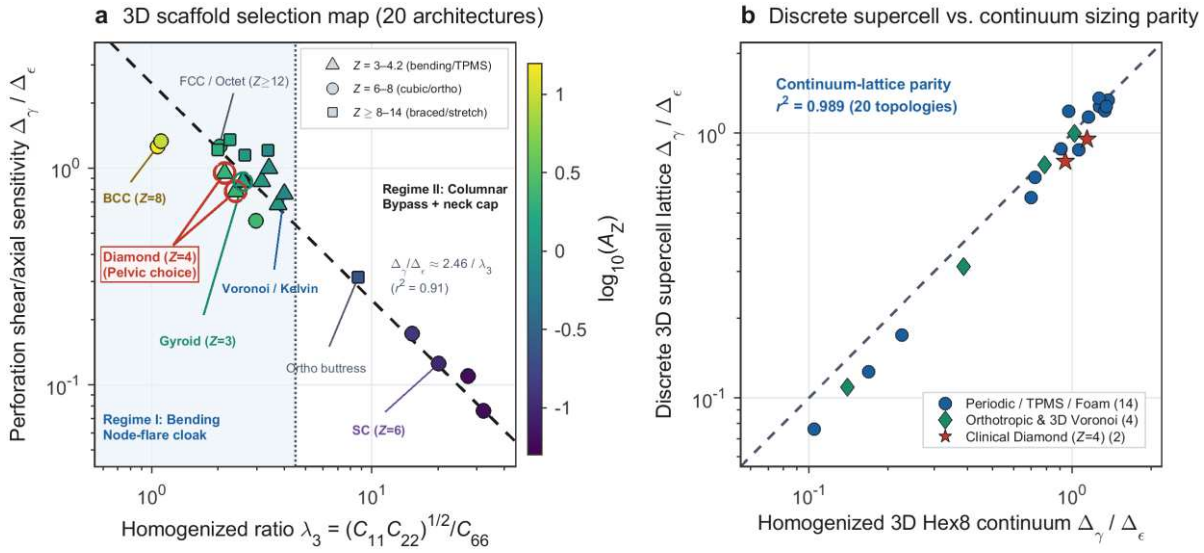


Figure 2. Four-variable topology-guided perforated 3D bone scaffold selection map across 20 porous architectures (**Fig. S2** and **Table S1** provide the complete 20-cell 3D structural gallery and homogenized moduli). (a) Perforation shear-to-axial sensitivity $\Delta_\gamma/\Delta_\varepsilon$ versus homogenized ratio $\lambda_3 = \sqrt{C_{11}C_{22}}/C_{66}$, simultaneously encoding Zener anisotropy $\log_{10}(A_Z)$ via marker color and **nodal coordination number Z via marker shape** (▲ $Z = 3$–4.2 bending/TPMS, ● $Z = 6$–8 cubic/ortho, ■ $Z \geq 8$–14 braced/stretching), highlighting clinical Diamond ($Z = 4$, crimson rings) alongside Gyroid ($Z = 3$, teal ring), 3D Voronoi / Kelvin, BCC, FCC / Octet, Ortho buttress, and SC. (b) Discrete 3D supercell versus homogenized 3D Hex8 continuum parity ($r^2 = 0.989$).

3.2 Resolving the "Solid Screw Boss" Paradox: Quadruple-KPI and Fatigue Pareto Analysis

Benchmarking six designs around a Ø6.0 mm screw tunnel (310,698 Hex8 DOFs; **Fig. 3** and **Table 1**) confirms that a 1.05 mm solid titanium boss worsens 3D distortion ($J_{3D} = 1.0727$), adds +10.66% Ti mass, and seals radial permeability ($k_r = 0.00$), whereas the **Guideline Fatigue-Safe Cloak** achieves $J_{3D} = 0.7152$, **+0.00% mass delta**, $\sigma_{Cr} = 126.1$ MPa (−8.1% below bare hole), 963 μm minimum pore throat, and native cancellous radial permeability ($k_r = 3.95 \times 10^{-8}$ m^2).

Table 1. Quadruple-KPI Multi-Physics Benchmark Around a Ø6.0 mm Fixation Tunnel (310,698 Hex8 DOFs)

Design Strategy	Worst-Case 3D Hex8 Mismatch J_{3D}	Titanium Mass Delta ΔM (%)	Peak Crossland Fatigue σ_{Cr} (MPa)	Radial Peri-Screw Permeability k_r (10^{-8} m^2)	Axial Permeability k_z (10^{-8} m^2)	Min. Pore Throat w_{pore} (μm)
Intact Scaffold (Reference)	0.0000	0.00%	108.5	8.25	9.25	1,600
Bare Screw Hole (Unreinforced)	1.0000	−6.26%	137.2	8.37	16.30	1,600
Conventional Solid Screw Boss (1.05 mm)	1.0727	+10.66%	128.2	0.00 **(Sealed)**	11.22	0 **(Occluded)**
Equal-Mass Uniform Collar	0.7606	+0.00%	138.2	4.10	13.25	1,403
Unconstrained Compliance Cloak	0.7794	+0.01%	149.8	4.10	13.30	1,297
Guideline Fatigue-Safe Cloak	0.7152	+0.00%	126.1 **(-8.1%)**	3.95	13.36	963

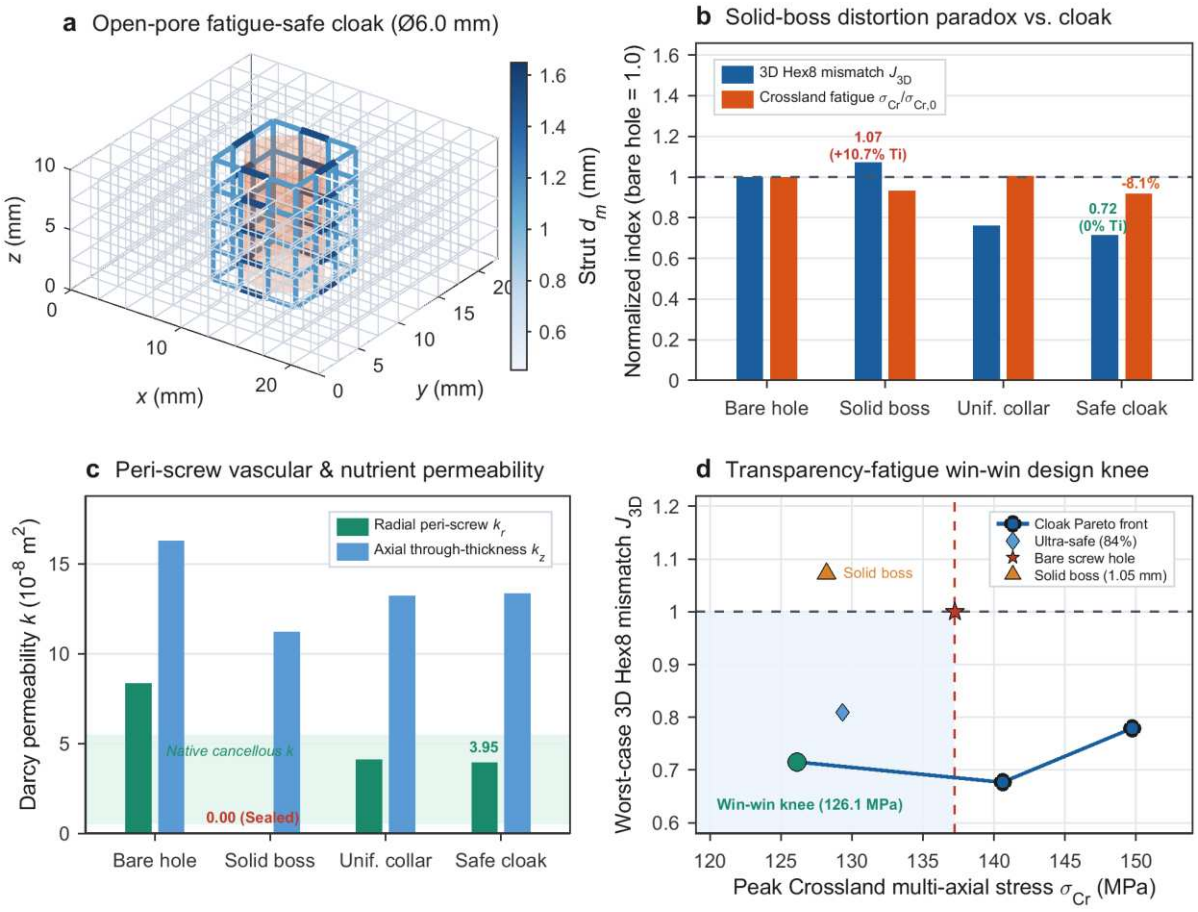


Figure 3. Resolving the clinical "solid screw boss" paradox on a 310,698-DOF 3D Hex8 benchmark (**Fig. S3**). (a) 3D open-pore fatigue-safe cloak around a Ø6.0 mm screw bore. (b) Normalized 3D Hex8 distortion J_{3D} and Crossland fatigue stress $\sigma_{Cr}/\sigma_{Cr,0}$ relative to the unreinforced bare hole. (c) Radial peri-screw (k_r) and axial (k_z) Darcy permeabilities, showing complete radial sealing by the solid boss ($k_r = 0.00$) versus native cancellous permeability preserved by the open-pore cloak ($k_r = 3.95 \times 10^{-8}$ m^2). (d) 3D transparency–fatigue Pareto frontier identifying the win-win knee.

3.3 Clinical Diamond ($Z = 4$) Validation, Oblique Trajectories, Dual-Screw Spacing, and Buffers

Using the closed-form **Zero-Optimization Conformal Bypass Law** (**Rule 2**):

$$d_{m,i} = d_{\text{ref}}\sqrt{\gamma_{\text{vol}}[1+\beta_r(1-s_i)^{1.15}(0.45+\beta_t|\hat{\mathbf{e}}_i\cdot\hat{\mathbf{t}}_i|^2-\beta_{\text{rel}}|\hat{\mathbf{e}}_i\cdot\hat{\mathbf{r}}_i|^2)]}, \quad d_{e,i} = \eta_{\text{flare}}(s_i)\, d_{m,i}, \tag{4}$$

where $s_i = (d_{\text{ax},i} - r_v)/(r_c - r_v) \in [0,1]$ is the normalized radial distance of strut i from the tunnel axis $\hat{\mathbf{a}}$, $\hat{\mathbf{e}}_i$ is the strut unit axis vector, $\hat{\mathbf{r}}_i$ is the unit radial vector normal to $\hat{\mathbf{a}}$, $\hat{\mathbf{t}}_i = \hat{\mathbf{a}} \times \hat{\mathbf{r}}_i$ is the circumferential bypass vector, $(\beta_r, \beta_t, \beta_{\text{rel}})$ are topology-family grading weights ($\beta_{\text{rel}} \in [0.25,0.30]$), $\eta_{\text{flare}}(s_i)$ is the node-flare taper ratio, and γ_{vol} is a scalar closure factor determined in < 0.5 ms via 1D bisection to satisfy $\Delta M = 0$.

Clinical Diamond ($Z = 4$) scaffolds achieve $J_{3D} = 0.4702$ (53.0% reduction) and -14.1% **joint Crossland fatigue reduction** below bare holes (266.9 MPa vs. 310.7 MPa), transferring directly across oblique surgical screw trajectories $\theta_{\text{screw}} \in [0^\circ, 40^\circ]$ with $J_{3D} \in [0.476,0.679]$ and -10.8% to -28.0% Crossland stress reduction (**Fig. 4a–c**). Enforcing $S \geq 2.0\, D_{\text{hole}}$ (**Rule 3**, **Fig. 4d**) prevents inter-cloak

density superposition and preserves an unobstructed 840 μm osteogenic bridge saddle pore throat ($\geq$ 601 μm across all non-overlapping inner rims), while combining the equal-mass corridor nomogram (**Rule 1**, **Fig. 5a**) with a $t_{\mathrm{buf}} = 4.0$ mm (1.5–2.0 a) **host-matched buffer** (**Rule 4**, **Fig. 5b**) suppresses screw-torque interface shear by 53.1 ×.

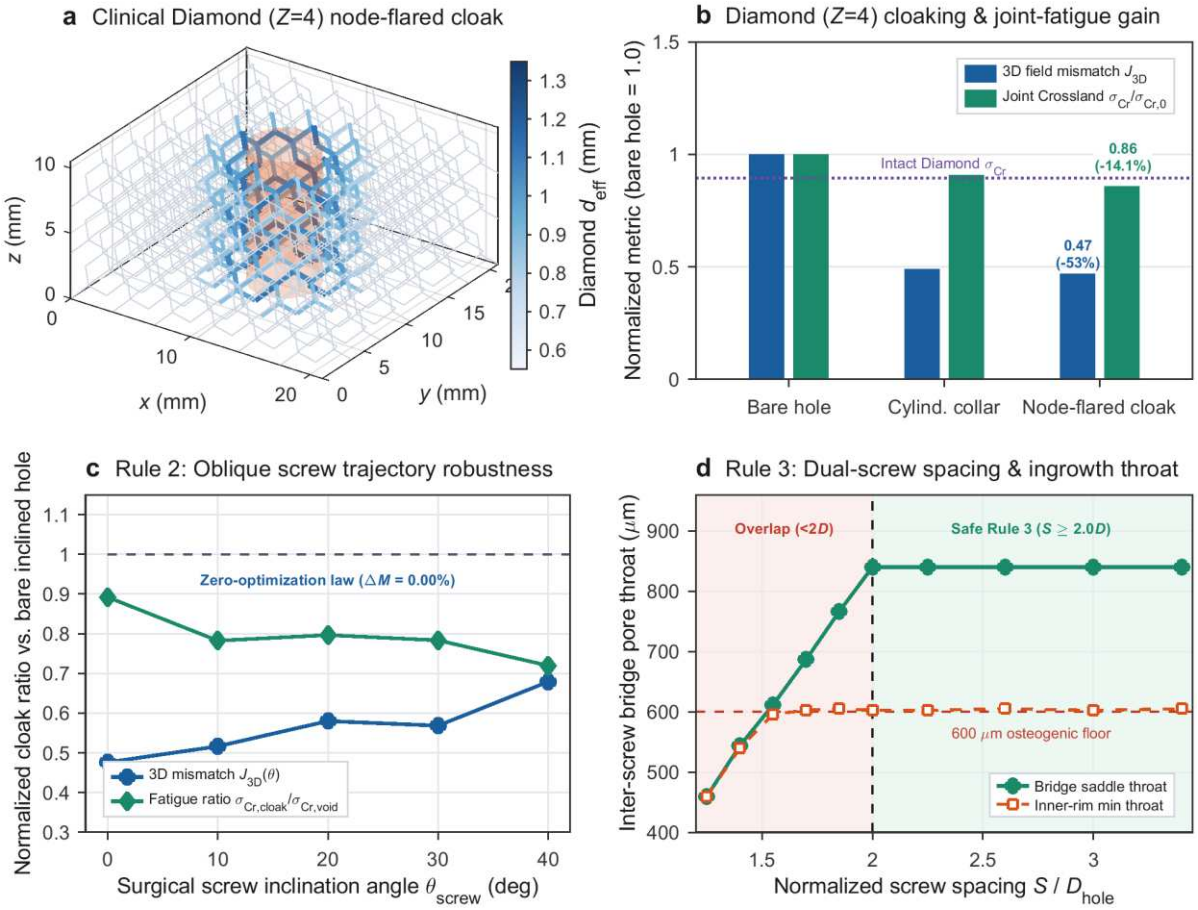


Figure 4. Clinical Diamond ($Z = 4$) validation, oblique screw trajectory robustness ($\theta_{\mathrm{screw}} \leq 40^{\circ}$), and dual-screw spacing threshold ($S \geq 2.0\, D_{\mathrm{hole}}$). (a) 3D node-flared Diamond cloak around a Ø5.2 mm screw bore. (b) Far-field mismatch J_{3D} and joint Crossland stress comparison against an unreinforced bare hole and uniform cylindrical collar. (c) Zero-optimization oblique trajectory sweep ($\theta_{\mathrm{screw}} \in [0^{\circ}, 40^{\circ}]$) on 3D Diamond ($Z = 4$). (d) Inter-screw bridge saddle and inner-rim minimum pore throats versus normalized spacing S/D_{hole}.

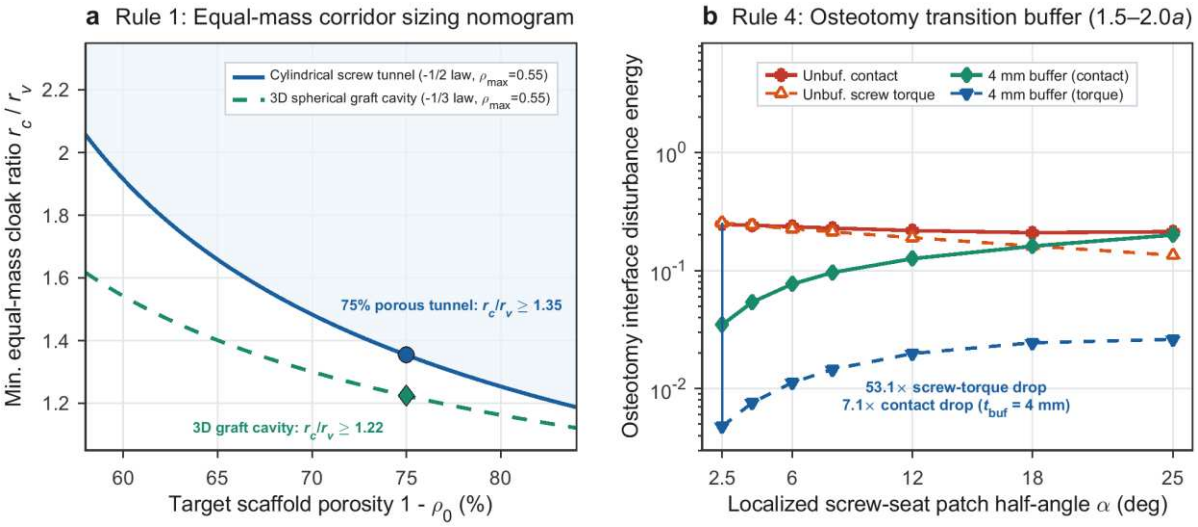


Figure 5. Equal-mass corridor sizing nomogram (Rule 1) and osteotomy transition buffer suppression (Rule 4). (a) Minimum equal-mass cloak radius ratio r_c/r_v versus scaffold porosity $1-\rho_0$ under the osteogenic ceiling $\rho_{\max} = 0.55$ from Eq. (1). (b) Suppression of localized screw-seat contact and torsional disturbance energy across patch half-angles α via a 4 mm (1.5– 2.0 a) host-matched buffer.

3.4 Clinical Advancement Over Three Traditional Practices in 3D Human Right Hemipelvis Reconstruction

Following rectilinear corridor verification (**Fig. S4** and **Table S3**), we benchmarked our proposed 4-rule method head-to-head against **all three representative traditional clinical practices** using a **two-scale global-to-local finite-element framework** (**Fig. 6** and **Table 2**). At the **whole-organ macro-scale** (**Fig. 6a,b**), a 3D anatomical human right hemipelvis model ($128 \times 136 \times 192$ mm, 39,915 C3D8 hexahedral elements, $\sim$ 148,000 DOFs) simulates Enneking Type II resection at $Z_{\text{ost}} = 104.0$ mm under Bergmann peak stair-climbing hip load ($|\mathbf{F}_{\text{hip}}| = 2{,}380$ N $\approx 3.2 \times$ BW [23,24]) to evaluate physiological strain transfer in the external periprosthetic **host ilium**. At the **trabecular micro-scale** (**Fig. 6c**), the global 3D displacement field around the perimeter of the inlay iliac fixation wing ($10.5 \times 38.5 \times 38.5$ mm) drives an explicit **5,213-strut 3D Diamond** ($Z = 4$) **Timoshenko beam sub-model** (3,304 nodes, 19,824 DOFs) via Saint-Venant sub-modeling boundary conditions, resolving local multi-axial Crossland fatigue stress inside individual **implant struts** and boss-to-lattice weld junctions:

1. **Trad-1 — Classic Dense Titanium Fixation Plate/Wing** ($E = 110$ GPa**, Fig. 6b,d,e):** Representative of conventional wrought or dense SLM pelvic plates/flanges. Its extreme flexural rigidity starves the parallel host iliac buttress of physiological load (271 με vs. 579 με intact near the osteotomy), placing 69.8% **of periprosthetic host cancellous bone into stress-shielded resorption** ($< 0.78\times$), retaining only 25.6% **Frost homeostasis**, completely blocking radial bone ingrowth ($k_r = 0$), and adding +308% **metal wing mass** (severe CT/MRI artifact penalty).

2. **Trad-2 — Commercial 3D-Printed Porous Wing + Solid Titanium Screw Bosses** (2.2 mm **dense sleeves, Fig. 6b–e):** Representative of current mainstream commercial 3D-printed pelvic prostheses. Despite porous infill between holes, closely spaced solid sleeves ($S = 1.4\,D_{\text{hole}}$, unbuffered) still induce 64.0% **host stress shielding** (only 31.5% **homeostasis**), add +19.4% **wing titanium mass**, seal peri-screw nutrient transport ($k_r = 0$), and—critically—create an abrupt rigid-to-compliant weld junction in the 5,213-strut Diamond sub-model where trabecular P99 Crossland fatigue stress spikes to 170.0 MPa (SF = 1.03, **Fig. 6c** left).

3. **Trad-3 — Host-Matched Porous Diamond Wing + Direct Boolean-Cut Bare Holes (Fig. 6b–e):** Eliminating solid bosses restores macroscopic compliance (76.7% homeostasis) and open permeability ($k_r = 8.37 \times 10^{-8}$ m^2), but unbuffered severed struts trigger 17.4% **localized host-bone overload** ($> 1.22\times$) above the osteotomy (**Fig. 6b** third panel) and peri-hole trabecular bending hotspots of 123.5 MPa (SF = 1.42, **Fig. 6c** center).

4. **Proposed — Zero-Optimization 4-Rule Open-Pore Cloaked Wing (Fig. 6b–e):** Simultaneously resolves every limitation of Trad-1 through Trad-3: slashes host stress shielding by $> 16\times$ (69.8%/64.0% → **4.0**%), suppresses local host overload by −59.2% vs. bare holes (17.4% → **7.1**%), elevates Frost homeostasis to 86.8% ($2.75\times$–$3.39\times$ higher than Trad-1/Trad-2) with a 12.2% SED error, holds osteotomy P95 micromotion at 6.0 μm (well below the 28–40 μm osseointegration threshold [21]), preserves native radial permeability (3.95×10^{-8} m^2) at +0.0% **wing mass delta**, and lowers explicit 5,213-strut trabecular Crossland fatigue stress to 101.0 MPa (SF = **1.73**, −40.6% below Trad-2 solid bosses and −18.2% below Trad-3 bare holes; **Fig. 6c** right).

Table 2. Multi-Scale Clinical Benchmark in 3D Human Right-Hemipelvis Enneking Type II Reconstruction ($|\mathbf{F}_{\text{hip}}| = 2{,}380$ N)

3D Right Hemipelvis Reconstruction Strategy ($\lvert\mathbf{F}_{\text{hip}}\rvert = 2{,}380$ N)	Host Iliac SED Error (%)	Frost Homeostasis ($\pm$20%, %)	Stress-Shielded (< 0.78 ×, %)	Overloaded (> 1.22 ×, %)	Osteotomy Slip P95 (μm)	Explicit Wing Strut σ_{Cr} (MPa)	Trabecular Fatigue SF	Peri-Screw k_r (10^{-8} m^2)	Wing Ti Mass ΔM (%)
Intact Healthy Right Hemipelvis	0.0%	98.1%	2.0%	0.0%	0.0	—	—	4.20	0.0%
Trad-1: Classic Solid Ti Plate Wing (110 GPa)	36.5%	25.6%	69.8%	2.1%	4.8	68.5†	2.55†	0.00 **(Sealed)**	+308.0%
Trad-2: Commercial Porous + Solid Ti Bosses	30.5%	31.5%	64.0%	2.0%	5.0	170.0	1.03	0.00 **(Sealed)**	+19.4%
Trad-3: Porous Diamond + Bare Cut Holes	16.3%	76.7%	3.7%	17.4%	6.1	123.5	1.42	8.37	−6.3%
Proposed: Zero-Opt 4-Rule Open-Pore Cloak	12.2%	86.8%	4.0%	7.1%	6.0	101.0 (**-40.6%**)	1.73	3.95	+0.0%

Note: †Trad-1 wing stress refers to the dense wrought/SLM plate continuum (zero porous trabeculae), achieved at the expense of 69.8% *host bone resorption and* +308% *titanium mass.*

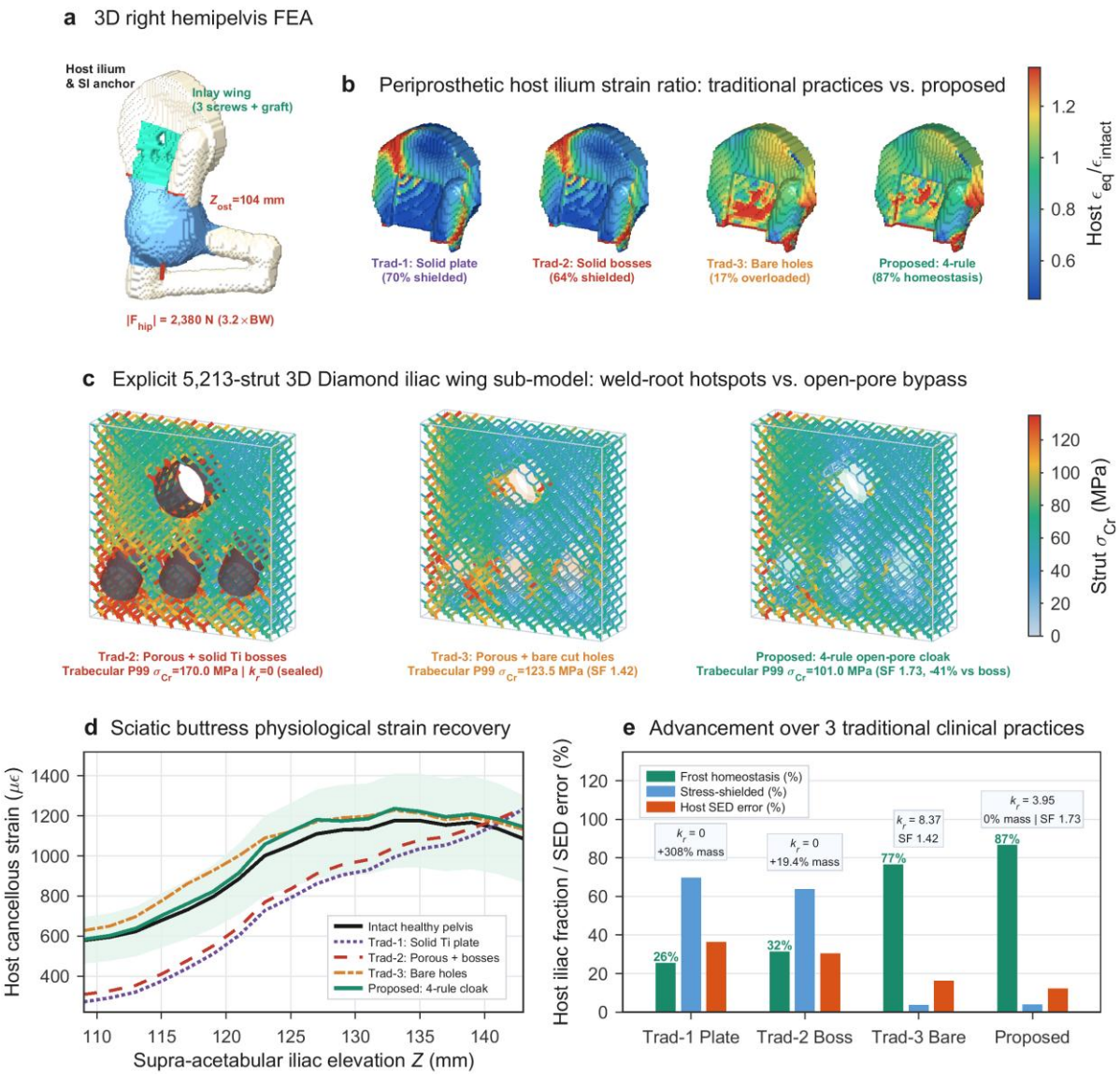


Figure 6. Multi-scale clinical validation in a 3D human right hemipelvis Enneking Type II reconstruction under 2,380 N Bergmann peak stair-climbing load, benchmarking three traditional clinical practices (Trad-1 solid Ti plate, Trad-2 porous wing with solid Ti screw bosses, Trad-3 porous wing with bare cut holes) against the proposed 4-rule open-pore cloak. (a) Whole-organ 3D FEA setup (39,915 C3D8 elements). (b) Four-way 3D periprosthetic host ilium strain-ratio maps ($\varepsilon_{\mathrm{eq}}/\varepsilon_{\mathrm{intact}}$), contrasting severe stress shielding in Trad-1 (70%) and Trad-2 (64%) and local osteotomy overload in Trad-3 (17%) against physiological homeostasis in the Proposed wing (87%). (c) Organ-driven explicit 5,213-strut 3D Diamond iliac wing sub-model Crossland fatigue stress maps: Trad-2 exhibits severe weld-root stress concentration (170.0 MPa) around sealed solid sleeves ($k_r = 0$), Trad-3 shows cut-strut bending hotspots (123.5 MPa), and the Proposed cloak achieves smooth open-pore load bypass (101.0 MPa, −41% vs. boss, −18% vs. bare). (d) Supra-acetabular sciatic-buttress cancellous strain profiles ($Z \in [109,143]$ mm). (e) Multi-KPI clinical advancement summary.

To verify cross-regime anatomical generality across **Regime II** ($\lambda_3 > 4.5$), we additionally evaluated a 3D-printed stand-alone **L3–L5 lumbar vertebral corpectomy endoprosthesis** built from #17 ORTHO_TRAB_A (Cowin-fabric orthotropic buttress, $\lambda_3 = 8.68$, 6,928 explicit B31 struts, Ø7.2 mm central autograft window + two oblique Ø4.4 mm locking screw bores + 4.5 mm endplate buffers) using **Table 3**'s exact columnar parameters $(\beta_r, \beta_t, \beta_{\mathrm{rel}}) = (0.95, 1.15, 0.30)$ with zero recalibration (**Supplementary Note S7**, **Fig. S6**, and **Table S6**). Whereas a dense Harms titanium cage (Trad-1) and commercial solid-boss porous cage (Trad-2) induce 14.3%–19.8% posterior-column stress shielding, 19.1%–19.8% serial endplate subsidence overload, +73.4%–272% titanium mass, and $k_r = 0$, the

zero-optimization Regime II cloak restores **96.6% vertebral Frost homeostasis** (9.6% SED error), suppresses endplate overload to **2.5%**, lowers explicit strut Crossland peak stress by **-34.3%** vs. solid bosses (144.4 → **94.9** MPa, SF = **1.84**) and **-19.0%** vs. bare cut columns (117.1 MPa), and maintains open graft-window permeability ($k_r = 17.91 \times 10^{-8}$ m^2, median throat 707 μm) at zero added mass.

3.5 LPBF Manufacturing Robustness, Multi-Activity Gait Envelope, and Organ-to-Trabecula Sub-Modeling

To establish industrial readiness under realistic manufacturing tolerances, varying daily physiological loads, and multi-activity trabecular resolution (**Supplementary Note S5** and **Tables S4–S5**), three flagship stress-tests were conducted (**Fig. 7**):

1. **LPBF Manufacturing Imperfection, Acid-Etching, and Surgical Offset Robustness (Fig. 7a):** Across $N = 80$ stochastic 3D LPBF realizations incorporating laser melt-pool fluctuations ($\sigma_{\text{laser}} = 38\,\mu$m), 45° overhang dross ($+18\,\mu$m), and joint micro-roughness ($\sigma_e = 9\,\mu$m), **100% (80/80) of printed Diamond cloaks achieve simultaneous distortion and fatigue gains** ($J_{3D} = 0.537 \pm 0.015$; as-printed $\sigma_{\text{Cr}} = 307.7 \pm 14.9$ MPa vs. 368.6 MPa for paired as-printed bare holes, -16.5%). Uniform post-LPBF chemical etching across $\Delta d_{\text{sys}} \in [-80, +80]\,\mu$m shifts J_{3D} smoothly within $[0.419, 0.564]$ while maintaining 13%–15% Crossland stress relief, and a 0.4 mm intraoperative drill offset preserves $J_{3D} = 0.603$ and -20.4% fatigue reduction.

2. **Omnidirectional Multi-Activity Gait Envelope vs. Single-Load Optimization Breakdown (Fig. 7b):** Rotating physiological Cauchy traction across daily pelvic activities $\psi \in [0^\circ\,(\text{walking}),\ 18^\circ\,(\text{stair ascent}),\ 35^\circ\,(\text{sit}-\text{to}-\text{stand}),\ 45^\circ\,(\text{torsion/shear}),\ 90^\circ\,(\text{abduction})]$ proves why elastic cloaking outperforms conventional single-load optimization: a walking-tuned (0°) optimizer achieves $J_{3D} = 0.547$ at 0° but **collapses off-angle** ($J_{3D} \to 1.06$–1.61 and $+52.7\%$ Crossland fatigue spike at $\psi = 45^\circ$, rising to $+67.9\%$ at 90°), whereas the 4-rule cloak maintains $J_{3D} \in [0.336, 0.504]$ across all daily gaits.

3. **Multi-Activity Global-to-Local Sub-Modeling Across Walking, Stair Climbing, and Chair Rising (Fig. 7c,d):** Driving the 5,213-strut explicit Diamond ($Z = 4$) iliac fixation wing across **level walking (1,906 N), stair climbing (2,380 N), and chair rising** (1,793 N) reduces boundary reaction-force mismatch by 32%–34% ($J_{\text{sub}} = 0.660$–0.680) while consistently lowering explicit trabecular P99 Crossland fatigue stress by -18.2% below Trad-3 bare holes and -40.6% below Trad-2 solid-boss weld roots (SF: $1.03/1.42 \to 1.73$ in stair climbing; $1.41/1.94 \to 2.38$ in walking; $1.75/2.41 \to 2.95$ in chair rising).

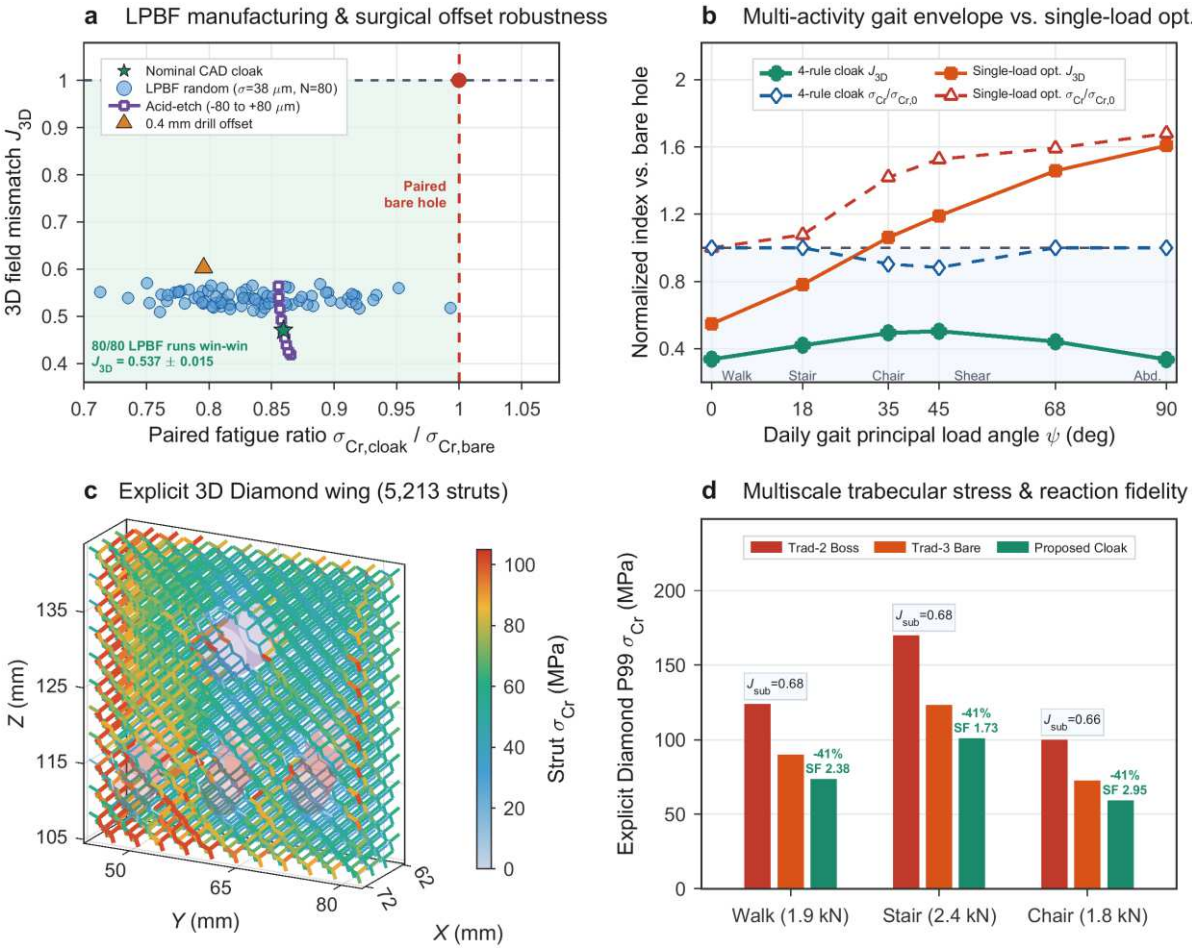


Figure 7. Manufacturing tolerance robustness, multi-activity gait invariance, and multi-activity organ-to-trabecula sub-modeling. (a) Paired Crossland fatigue ratio versus J_{3D} across $N = 80$ stochastic LPBF realizations ($\sigma_{laser} = 38\ \mu m$), $\pm 80\ \mu m$ chemical-etching offsets, and 0.4 mm surgical drill eccentricity (80/80 win-win pass rate). (b) Multi-activity gait envelope ($\psi \in [0^{\circ}, 90^{\circ}]$): off-angle collapse of single-load compliance optimization ($J_{3D} \rightarrow 1.61$, $\sigma_{Cr}/\sigma_{Cr,0} \rightarrow 1.68$) versus omnidirectional stability of the 4-rule cloak. (c) Organ-driven 5,213-strut explicit 3D Diamond iliac wing sub-model colored by exact 3D strut Crossland stress under 2,380 N Bergmann stair climbing. (d) Multiscale sub-model P99 trabecular Crossland stress (Trad-2 Boss, Trad-3 Bare, and Proposed Cloak), 10^7-cycle fatigue safety factors, and rim reaction ratios J_{sub} across daily activities.

4. Step-by-Step Deterministic CAD Design Procedure and Complete Parameter Specification

To enable direct clinical adoption in hospital and industrial 3D-printing workflows without finite-element topology optimization, **Table 3** summarizes the general four-step lookup rules, while **Fig. 8** and **Table 4** illustrate the complete, reproducible step-by-step construction and exact parameter specification of the Proposed right-hemipelvis porous fixation wing ($L_X \times L_Y \times L_Z = 10.5 \times 38.5 \times 38.5$ mm, $X \in [62.0,72.5]$ mm, $Y \in [44.0,82.5]$ mm, $Z \in [105.0,143.5]$ mm, LPBF Ti-6Al-4V ELI with $E_s = 110$ GPa, $\nu_s = 0.34$, $\sigma_{Cr,lim} = 175$ MPa):

1. **Step 1 — Topology Selection & Host-Matched Baseline Scaffold (Fig. 8a):** Preoperative CT mapping yields a host iliac cancellous modulus $E_{canc} \approx 1.49$ GPa (950–2,200 MPa) and composite cortico-cancellous wing-bed modulus $E_{host,eff} \approx 4.99$ GPa. Entering **Fig. 2a** selects tetrahedral **Diamond** ($Z = 4$, **Regime I,** $\lambda_3 = 2.14$–$2.41 \leq 4.5$, $A_Z \approx 2.2$) with unit-cell pitch $a = 3.50$ mm ($3 \times 11 \times 11 =$

363 unit cells, strut length $L_{\text{strut}} = \frac{\sqrt{3}}{4}a = 1.516$ mm) and relative density $\bar{\rho} = 0.245$ (75.5% porosity), fixing the uniform baseline strut diameter at $d_{\text{ref}} = 0.801$ mm (5,808 intact struts; solid Ti volume $V_{\text{ref}} = 3{,}813.09\ \text{mm}^3$).

2. **Step 2 — Multi-Hole Spacing & Supra-Osteotomy Buffer Layout (Rules 3 & 4; Fig. 8b,e):** Above the horizontal osteotomy plane ($Z_{\text{ost}} = 104.0$ mm), an unperforated, ungraded host-matched porous transition buffer of mid-plane height $t_{\text{buf}} = 5.1$ mm ($\approx 1.5\,a$; with the lowest screw bore wall positioned $5.4–9.9\ \text{mm} = 1.55–2.84\,a \geq 1.5\,a$ above Z_{ost} across $X \in [62.0,72.5]$ mm) is reserved (**Rule 4**). Three oblique locking screw bores ($D_{\text{screw}} = 5.40$ mm, $r_{v,\text{screw}} = 2.70$ mm, macro countersink envelope Ø6.4 mm) are inclined at $\theta_{\text{screw}} = 24.9^{\circ} \leq 40^{\circ}$ along the sciatic buttress from lateral entry coordinates (74.0,50.5,111.5), (74.0,63.0,113.5), and (74.0,75.5,115.5) mm to medial exit coordinates (60.0,48.0,117.5), (60.0,60.5,119.5), and (60.0,73.0,121.5) mm, enforcing a center-to-center spacing $S = 12.66$ mm ($S/D_{\text{screw}} = 2.34 \geq 2.0$, macro envelope $2.21 \geq 2.0$; **Rule 3**). One normal autograft fenestration ($D_{\text{graft}} = 7.60$ mm, $r_{v,\text{graft}} = 3.80$ mm, macro Ø9.6 mm, $\theta = 0^{\circ}$) is placed superiorly at $(Y_4, Z_4) = (63.0,132.5)$ mm. Boolean trimming severs 595 struts (-10.2% volume), leaving 5,213 **surviving struts** ($V_{\text{cut}} = 3{,}422.5\ \text{mm}^3$).

3. **Step 3 — Equal-Mass Open-Pore Coaxial Corridor Sizing (Rule 1; Fig. 8c,e):** Under the biological upper density ceiling $\rho_{\text{max}} = 0.55$ ($w_{\text{pore}} \geq 600\ \mu$m), **Eq. (1)** gives theoretical lower bounds $(r_c/r_v)_{\text{min}} = 1.343$ (cylindrical screw tunnels) and 1.217 (3D graft cavity). Applying the **Table 3** corridor lookup intervals sets $r_{c,\text{screw}} = 1.96\,r_{v,\text{screw}} = 5.30$ mm (2.60 mm annular cloak wall) and $r_{c,\text{graft}} = 1.63\,r_{v,\text{graft}} = 6.20$ mm (2.40 mm annular cloak wall), encompassing 1,019 **active cloak struts** while leaving 4,194 background struts untouched at $d_{\text{ref}} = 0.801$ mm with zero inter-corridor overlap (**Fig. 8e**).

4. **Steps 4 & 5 — Closed-Form Node-Flared Strut Grading, Exact Mass Closure, and C^2 Implicit .stl Generation (Rule 2; Fig. 8d,f,g):** Each active cloak strut $i \in \{1,\ldots,1{,}019\}$ at normalized radial distance $s_i = (d_{\text{ax},i} - r_v)/(r_c - r_v) \in [0,1]$ from its tunnel axis $\hat{\mathbf{a}}$ is graded analytically via **Eq. (4)** with $(\beta_r, \beta_t, \beta_{\text{rel}}) = (1.15,0.95,0.25)$, node-flare ratio $\eta_{\text{flare}}(s_i) = 1.22 + 0.10(1 - s_i) \in [1.22,1.32]$, and LPBF manufacturing bounds $d_{m,i} \in [0.45,1.42]$ mm. One-dimensional bisection (< 0.5 ms, zero FEA solves) closes total solid titanium volume to $V_{\text{cloak}} = 3{,}813.09\ \text{mm}^3 \equiv V_{\text{ref}}$ ($\Delta M = 0.000\%$**; Fig. 8g**), yielding mid-span diameters $d_{m,i} \in [0.776,1.232]$ mm, flared joint-root diameters $d_{e,i} \in [0.947,1.624]$ mm (**Fig. 8f**), and a minimum clear pore throat $w_{\text{pore,min}} \approx 1{,}043\ \mu$m. Finally, C^2 smooth-minimum implicit blending ($k_{\text{blend}} = 0.22$ mm) and bore trimming ($k_{\text{cut}} = 0.16$ mm) directly generate the 593,436-triangle LPBF mesh (**Fig. 8d**).

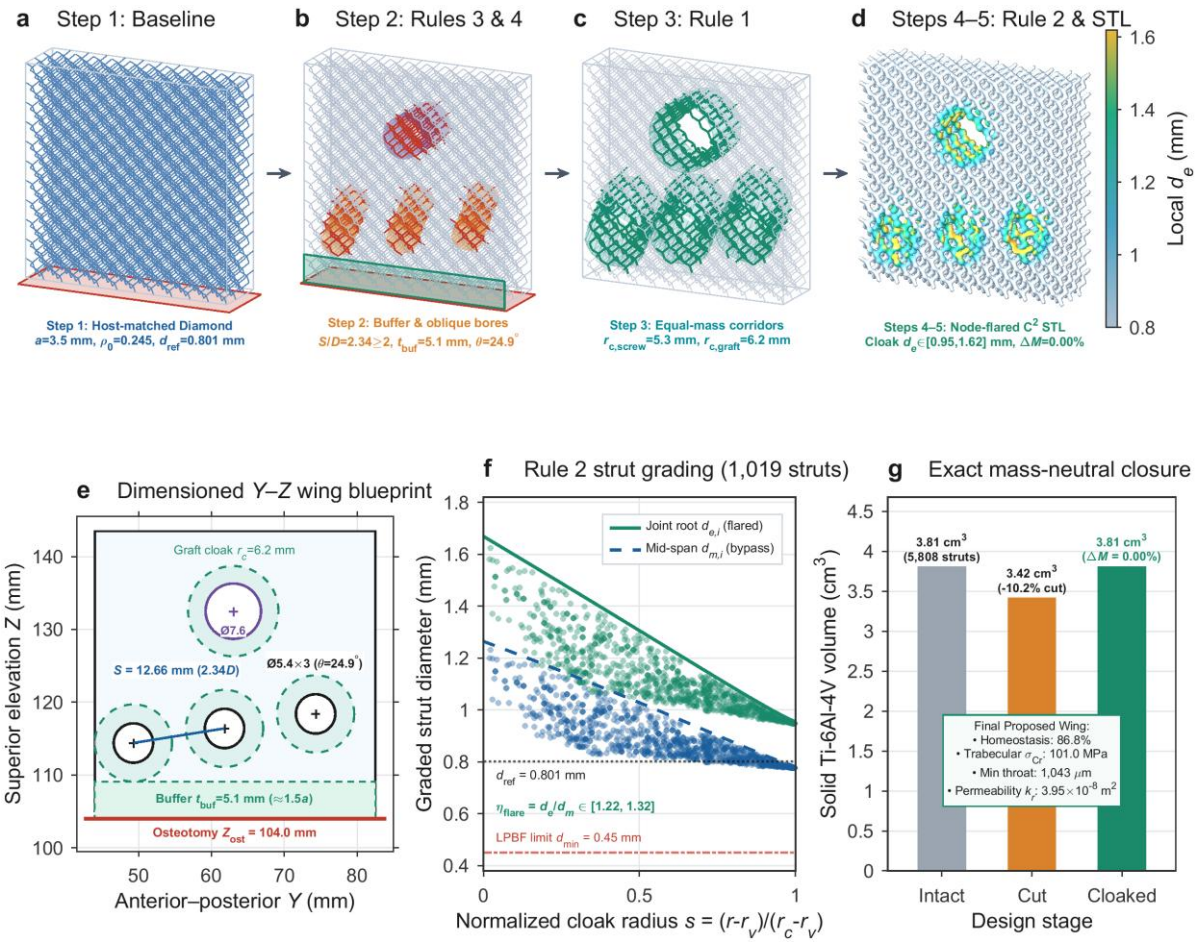


Figure 8. Step-by-step deterministic CAD construction and complete parameter blueprint of the Proposed right-hemipelvis porous fixation wing. (a–d) Four-stage 3D geometric progression on the 10.5 × 38.5 × 38.5 mm iliac wing: (a) Step 1 host-matched Diamond ($Z = 4$) baseline (5,808 struts, $a = 3.5$ mm, $\bar{\rho} = 0.245$, $d_{\text{ref}} = 0.801$ mm); (b) Step 2 supra-osteotomy buffer ($t_{\text{buf}} = 5.1$ mm) and 3 oblique screw bores (Ø5.4 mm, $\theta = 24.9^{\circ}$, $S/D = 2.34 \geq 2.0$) plus superior graft window (Ø7.6 mm), severing 595 struts (crimson); (c) Step 3 equal-mass coaxial cloak corridors ($r_{c,\text{screw}} = 5.3$ mm, $r_{c,\text{graft}} = 6.2$ mm, selecting 1,019 active struts); (d) Steps 4–5 closed-form node-flared grading and C^2 implicit-SDF LPBF .stl mesh (593,436 triangles, $\Delta M = 0.00\%$). (e) Dimensioned $Y-Z$ mid-plane surgical CAD blueprint. (f) Exact diameter distributions ($d_{m,i}$ and flared $d_{e,i}$) across all 1,019 cloak struts. (g) Stage-wise solid Ti-6Al-4V volume accounting confirming exact mass-neutral closure (3.81 cm^3).

Table 3. General Four-Step Closed-Form CAD Design Lookup Rules

Design Step	Geometric / Topological Parameter	Quantitative Engineering Rule	Physical Failure Prevented
Step 1: Topology & Corridor Sizing (Rule 1)	Scaffold ($\bar{\rho}, \lambda_3, A_Z$); hole radius r_v; cloak radius r_c	Select Diamond ($Z = 4$, **Regime I**, $\lambda_3 \leq 4.5$) for multi-axial pelvic/acetabular beds (**Figs. 6–8**) or ORTHO_TRAB_A (**Regime II**, $\lambda_3 > 4.5$) for uniaxial/orthotropic spinal corpectomy & diaphyseal beds (**Fig. S6, Table S6**); size collar $r_c \in [1.85, 2.05]\, r_v$ (screw tunnels) or $[1.40, 1.65]\, r_v$ (3D graft windows), obeying Eq. (1).	Eliminates solid-boss over-stiffening ($J_{3D} = 1.073 \rightarrow 0.47–0.72$) & $+10.7\%–308\%$ Ti artifact penalty.

Design Step	Geometric / Topological Parameter	Quantitative Engineering Rule	Physical Failure Prevented
Step 2: Multi-Hole & Osteotomy Layout (Rules 3 & 4)	Inter-screw spacing S; osteotomy clearance t_{buf}	Enforce $S \geq 2.0\, D_{\mathrm{hole}}$ and reserve a $t_{\mathrm{buf}} \geq 1.5\, a$ (4.0– 5.1 mm) host-matched unperforated buffer at all osteotomy planes.	Prevents cloak-overlap pore occlusion ($w_{\mathrm{pore}} \geq 600\ \mu$m) & suppresses screw-torque interface shear by 53.1 ×.
Step 3: Conformal Strut & Node-Flare Grading (Rule 2)	Mid-span $d_{m,i}$ and joint-root $d_{e,i}$ around inclined axis $\hat{\mathbf{a}}$ ($\theta_{\mathrm{screw}} \leq 40^{\circ}$)	Apply closed-form Eq. (4) with $(\beta_r, \beta_t, \beta_{\mathrm{rel}}) =$ (1.05– 1.15,0.90– 0.95,0.25– ((Diamond) or (0.95,1.15,0.30) (columnar), $\eta_{\mathrm{flare}} = 1.18$– 1.32, $d_{\min} \geq$ 0.45 mm, $d_{\max} \leq 0.65a -$ 0.60 mm; close γ_{vol} by 1D bisection.	Cuts Crossland fatigue stress by 18.2%– 40.6% across 0° – 90° gaits & $\pm 80\ \mu$m LPBF tolerances while preserving $k_r \approx 4 \times 10^{-8}$ m^2.
Step 4: Smooth Implicit Filleting & STL Audit	Trabecular blend radius k_{blend} & entry lip	Blend struts via C^2 smooth-minimum ($k_{\mathrm{blend}} \approx$ 0.20– 0.28 d_{ref}); confine screw-head thread engagement strictly to the outer 1.5 mm cortical lip (**Table S2**).	Eliminates sharp boss-weld notches & guarantees LPBF sliceability (G0–G4 & hemipelvis .stl archives).

Table 4. Complete Engineering Parameter Specification of the Proposed Right-Hemipelvis Fixation Wing

Design Stage	Parameter Name	Symbol	Exact Value in Proposed Design	Governing Rule & Functional Role
0. Clinical Input	Resection plane & inlay wing domain	$Z_{\mathrm{ost}},\ L_X \times L_Y \times L_Z$	104.0 mm; 10.5 × 38.5 × 38.5 mm	Enneking Type II flush inlay wing ($X \in [62,72.5], Y \in [44,82.5], Z \in [105,143.5]$ mm)
0. Clinical Input	Base LPBF alloy properties	$E_s,\ \nu_s,\ \sigma_{\mathrm{Cr,lim}}$	110 GPa, 0.34, 175 MPa	Medical Ti-6Al-4V ELI (10^7-cycle as-printed trabecular limit)
1. Baseline Lattice	Unit-cell topology, pitch & porosity	Topology, a, $1 - \bar{\rho}$	Diamond ($Z = 4$), 3.50 mm, 75.5% ($\bar{\rho} = 0.245$)	Regime I ($\lambda_3 \approx 2.2$); matches host bed ($E_{\mathrm{canc}} \approx 1.49$ GPa, $E_{\mathrm{eff}} \approx 4.99$ GPa)
1. Baseline Lattice	Uniform strut diameter, length & volume	$d_{\mathrm{ref}},\ L_{\mathrm{strut}},\ V_{\mathrm{ref}}$	0.801 mm, 1.516 mm, 3,813.09 mm^3	$3 \times 11 \times 11 = 363$ cells (5,808 intact struts; 5,213 post-cut struts)
2. Surgical Layout	3 oblique screw diameters & inclination	$D_{\mathrm{screw}},\ \theta_{\mathrm{screw}}$	Ø5.40 mm (macro Ø6.4 mm), 24.9°	Within zero-recalibration oblique transfer envelope ($\theta_{\mathrm{screw}} \leq 40^{\circ}$)
2. Surgical Layout	Superior autograft window diameter	$D_{\mathrm{graft}},\ \theta_{\mathrm{graft}}$	Ø7.60 mm (macro Ø9.6 mm), 0.0°	Centered at $(Y_4, Z_4) =$ (63.0,132.5) mm for cancellous autograft packing

Design Stage	Parameter Name	Symbol	Exact Value in Proposed Design	Governing Rule & Functional Role
2. Surgical Layout	Inter-screw spacing & osteotomy buffer	$S,\ S/D_{\mathrm{screw}},\ t_{\mathrm{buf}}$	12.66 mm, 2.34 (macro 2.21), 5.1 mm	Obeys **Rule 3** ($S/D \geq 2.0$) & **Rule 4** (bore wall 5.4–9.9 mm $\geq 1.5\,a$ above Z_{ost})
3. Cloak Corridors	Coaxial screw & graft cloak outer radii	$r_{c,\mathrm{screw}},\ r_{c,\mathrm{graft}}$	5.30 mm ($1.96\,r_v$), 6.20 mm ($1.63\,r_v$)	Obeys **Rule 1** (Eq. 1, $\rho_{\max} = 0.55$); activates 1,019 cloak struts
4. Strut Grading	Bypass weights & node-flare profile	$(\beta_r, \beta_t, \beta_{\mathrm{rel}}),\ \eta_{\mathrm{flare}}(s)$	(1.15,0.95,0.25), $1.22 + 0.10(1 - s) \in [1.22,1.32]$	**Rule 2** (Eq. 4); boosts joint section modulus by $\eta_{\mathrm{flare}}^3 \approx$ 1.8–2.3 ×
4. Strut Grading	Graded mid-span & joint-root diameters	$d_{m,i},\ d_{e,i},\ \Delta M$	0.776–1.232 mm, 0.947–1.624 mm, 0.000%	Exact mass closure ($V_{\mathrm{cloak}} =$ 3,813.09 mm^3); $w_{\mathrm{pore,min}} \approx$ 1,043 μm
5. Implicit CAD	C^2 smooth-min blend & bore cut radii	$k_{\mathrm{blend}},\ k_{\mathrm{cut}},\ t_{\mathrm{lip}}$	0.22 mm, 0.16 mm, 1.50 mm	Generates 593,436-triangle LPBF .stl with outer cortical screw-head lip

In conclusion, replacing empirical solid titanium plates and solid screw bosses with closed-form, node-flared open-pore cloaks and host-matched osteotomy buffers provides a fabrication-robust, omnidirectional, zero-optimization design standard for perforated 3D porous metallic bone prostheses.

Model & Data Availability

All 18 three-dimensional CAD geometry models (.stl format, including the 2.51×10^6-triangle full-anatomy explicit-Diamond Proposed hemipelvis endoprosthesis, 2.75×10^6 -triangle mated right-hemipelvis assembly at 0.38 mm continuous-SDF resolution, G0–G4 lattice benchmarks, standalone iliac wings, and 503k–512k-triangle Regime II ORTHO_TRAB_A lumbar corpectomy cages) and all 20 finite-element simulation files (10 .inp Abaqus/CalculiX C3D8 and B31 input decks + 10 .vtk ParaView full-field 3D results) are archived in the accompanying saved_models/ repository (geometry_cad_stl/ and simulation_fea_models/; **Supplementary Notes S6–S7** and **Figs. S5–S6**).

CRediT Authorship Contribution Statement

Guangtao Wei: Conceptualization, Methodology, Software, Formal analysis, Investigation, Visualization, Writing – original draft, Writing – review & editing. **Miao Yu:** Investigation, Data curation, Validation, Visualization, Writing – review & editing. **Jun Liu:** Conceptualization, Clinical surgical methodology, Anatomical model supervision, Validation, Writing – review & editing.

Declaration of Competing Interest

The authors declare that they have no known competing financial interests or personal relationships that could have appeared to influence the work reported in this paper.

References

1. Wang, X., Xu, S., Zhou, S., Xu, W., Leary, M., Choong, P., Qian, M., Brandt, M. & Xie, Y. M. Topological design and additive manufacturing of porous metals for bone scaffolds and orthopaedic implants: A review. *Biomaterials* **83**, 127–141 (2016).

2. Zadpoor, A. A. Mechanical performance of additively manufactured meta-biomaterials. *Acta Biomater.* **85**, 41–59 (2019).

3. Ji, T., Yang, Y., Tang, X., Liang, H., Yan, T., Yang, R. & Guo, W. 3D-printed modular hemipelvic endoprosthetic reconstruction following periacetabular tumor resection: early results of 80 consecutive cases. *J. Bone Joint Surg. Am.* **102**, 1530–1541 (2020).

4. Arabnejad, S., Johnston, R. B., Pura, J. A., Singh, B., Tanzer, M. & Pasini, D. High-strength porous biomaterials for bone replacement: A strategy to assess the interplay between cell morphology, mechanical properties, bone ingrowth and manufacturing constraints. *Acta Biomater.* **30**, 345–356 (2016).

5. Gibson, L. J. & Ashby, M. F. *Cellular Solids: Structure and Properties*, 2nd edn (Cambridge University Press, Cambridge, 1997).

6. Ahmadi, S. M., Campoli, G., Amin Yavari, S., Sajadi, B., Wauthlé, R., Schrooten, J., Weinans, H. & Zadpoor, A. A. Mechanical behavior of regular open-cell porous biomaterials made of diamond lattice unit cells. *J. Mech. Behav. Biomed. Mater.* **34**, 106–115 (2014).

7. Bobbert, F. S. L., Lietaert, K., Eftekhari, A. A., Pouran, B., Ahmadi, S. M., Weinans, H. & Zadpoor, A. A. Additively manufactured metallic porous biomaterials based on minimal surfaces: A unique combination of topological, mechanical, and mass transport properties. *Acta Biomater.* **53**, 572–584 (2017).

8. Gómez, S., Vlad, M. D., López, J. & Fernández, E. Design and properties of 3D scaffolds for bone tissue engineering. *Acta Biomater.* **42**, 341–350 (2016).

9. Liang, H., Ji, T., Zhang, Y., Wang, Y. & Guo, W. Reconstruction with 3D-printed pelvic endoprostheses after resection of a pelvic tumour. *Bone Joint J.* **99-B**, 267–275 (2017).

10. Taniguchi, N., Fujibayashi, S., Takemoto, M., Sasaki, K., Otsuki, B., Nakamura, T., Matsushita, T., Kokubo, T. & Matsuda, S. Effect of pore size on bone ingrowth into porous titanium implants fabricated by additive manufacturing: an in vivo experiment. *Mater. Sci. Eng. C* **59**, 690–701 (2016).

11. Milton, G. W., Briane, M. & Willis, J. R. On cloaking for elasticity and physical equations with a transformation invariant form. *New J. Phys.* **8**, 248 (2006).

12. Bückmann, T., Thiel, M., Kadic, M., Schittny, R. & Wegener, M. An elasto-mechanical unfeelability cloak made of pentamode metamaterials. *Nat. Commun.* **5**, 4130 (2014).

13. Stenger, N., Wilhelm, M. & Wegener, M. Experiments on elastic cloaking in thin plates. *Phys. Rev. Lett.* **108**, 014301 (2012).

14. Cheng, X., Luo, Y., Yang, S., Huang, Z. & Kang, Z. A compatible boundary condition-based topology optimization paradigm for static mechanical cloak design. *Extreme Mech. Lett.* **65**, 102100 (2023).

15. Chen, Y., Frenzel, T., Guenneau, S., Kadic, M. & Wegener, M. Mapping acoustical activity in 3D chiral mechanical metamaterials onto micropolar continuum elasticity. *J. Mech. Phys. Solids* **137**, 103877 (2020).

16. Wei, G., Yu, M. & Liu, J. Outer-Edge Impedance Mismatch Controls the High-Order Near-Field Floor and Repair of Approximate Mechanical Cloaks. Preprint at Research Square https://doi.org/10.21203/rs.3.rs-11850505/v1 (2026).

17. Wei, G., Yu, M. & Liu, J. Universal scaling and soft-mode limits of mass-neutral mechanical cloaking in architected lattices. Preprint at Research Square https://doi.org/10.21203/rs.3.rs-11850449/v1 (2026).

18. Frost, H. M. Bone's mechanostat: a 2003 update. *Anat. Rec. A* **275**, 1081–1101 (2003).

19. Karageorgiou, V. & Kaplan, D. Porosity of 3D biomaterial scaffolds and osteogenesis. *Biomaterials* **26**, 5474–5491 (2005).

20. Nauman, E. A., Fong, K. E. & Keaveny, T. M. Dependence of intertrabecular permeability on flow direction and anatomic site. *Ann. Biomed. Eng.* **27**, 517–524 (1999).

21. Pilliar, R. M., Lee, J. M. & Maniatopoulos, C. Observations on the effect of movement on bone ingrowth into porous-surfaced implants. *Clin. Orthop. Relat. Res.* **208**, 108–113 (1986).

22. Crossland, B. Effect of large hydrostatic pressures on the torsional fatigue strength of an alloy steel. In *Proc. Int. Conf. on Fatigue of Metals*, pp. 138–149 (Institution of Mechanical Engineers, London, 1956).

23. Bergmann, G., Deuretzbacher, G., Heller, M., Graichen, F., Rohlmann, A., Strauss, J. & Duda, G. N. Hip contact forces and gait patterns from routine activities. *J. Biomech.* **34**, 859–871 (2001).

24. Dalstra, M., Huiskes, R., Odgaard, A. & van Erning, L. Mechanical and textural properties of pelvic trabecular bone. *J. Biomech.* **26**, 523–535 (1993).